



Cite this: DOI: 10.1039/c8ta10554e

Two-dimensional extended π -conjugated triphenylene-core covalent organic polymer†

Xiao-Liang Ye,^a Yu-Qian Huang,^a Xing-Yan Tang,^a Juan Xu,^a Chengxin Peng^{*bcd} and Yuan-Zhi Tan^{id} ^{*a}

Carbon-rich two-dimensional (2D) materials show significant potential in energy storage and conversion applications. A conjugated 2D covalent organic polymer (COP) with embedded triphenylene (TP) units was synthesized by Glaser–Hay cross-coupling and validated by Raman, IR, XPS and NMR spectroscopy. TP-COP exhibited a uniform pore size of 5.4 Å and laminar structure with an interlayer spacing of 3.8 Å, which could be mechanically exfoliated to yield few-layered nanosheets. Interfacial polymerization produced the continuous TP-COP films from quasi-monolayer to multilayer. As the anode materials of lithium batteries, TP-COP delivered large reversible capacity up to 1624 mA h g⁻¹, high charge rate, and good recycling ability. These properties are likely due to the presence of lithium ions in both the interspace of the expanded sp² moieties and the in-plane nanopores of TP-COP.

Received 2nd November 2018
Accepted 18th December 2018

DOI: 10.1039/c8ta10554e

rsc.li/materials-a

Introduction

Two-dimensional (2D) materials have been of great interest since the rise of graphene,^{1–5} among which 2D covalent organic polymers (2D-COPs) have already been under extensive investigation.^{6–9} Compared with graphene, 2D-COPs are rationally synthesized by polymerization of designed monomers. Consequently, their structural units are atomically well-defined, which renders them tuneable and functionally oriented with diverse potential applications such as electrocatalysis^{10,11} and energy storage.^{6,12} Generally, dynamic covalent bonding is required to build highly ordered 2D-COPs, which are also commonly classified as covalent organic frameworks (COFs) because the reversible bonding/dissociation of dynamic covalent bonds repairs potential errors and defects that occur during polymerization.^{7,8,12} However, 2D-COFs constructed from dynamic covalent bonds suffer from instability originating from the bonding/dissociation equilibrium as well.⁷

Furthermore, C–C couplings including aromatic and alkyne C–C couplings have been widely used for the synthesis of one-dimensional conjugated polymers.¹³ The strong and

irreversible C–C bonds make these conjugated polymers highly stable.^{14,15} In recent years, a few 2D-COPs formed by C–C coupling have also been synthesized and investigated.^{13,15–20} Although 2D-COPs formed by polymerization through C–C bonds are generally less crystalline, C–C coupling can easily build a fully conjugated framework, where the π electrons are considerably delocalized. This delocalized electronic feature in these COPs ensures their superior charge transport and electrochemical properties.^{8,21}

One of the most famous COPs connected by C–C bonds is graphdiyne (GDY), a kind of 2D fully carbon-conjugated COP, which is synthesized by multiple Glaser–Hay alkyne C–C couplings of hexaethynylbenzene (HEB).²² Due to the conjugated framework, GDY is electrochemically active^{22,23} and has been applied in energy conversion^{24–26} and energy storage.^{27,28} The HEB units in GDY contain one benzenoid ring and six acetylenes. Fusing three additional benzenoid rings to the HEB units produces hexaethynyltriphenylene (HETP). Topologically, HETP has compatible molecular symmetry with a 2D hexagonal lattice and can replace HEB as the building block to construct graphene-like 2D COPs.

Herein, we report the synthesis of a triphenylene-embedded covalent organic polymer (TP-COP) using HETP as the monomer. TP-COP can be considered as a GDY analogue with expanded sp²-moieties (Fig. 1a). The chemical structure of TP-COP was characterized by NMR, Raman and X-ray photoelectron spectroscopy (XPS). The expanded sp² cores in TP-COP result in an enlarged pore size of 5.4 Å, which is larger than that of GDY (2.5 Å).²³ Notably, bulk TP-COP can be mechanically exfoliated into few-layered nanosheets, which is probably due to increased rigidity of the conjugated framework. Furthermore, the interfacial polymerization produced uniform and

^aState Key Laboratory for Physical Chemistry of Solid Surfaces, Collaborative Innovation Center of Chemistry for Energy Materials, Department of Chemistry, College of Chemistry and Chemical Engineering, Xiamen University, Xiamen 361005, China. E-mail: yuqian_huang@xmu.edu.cn

^bSchool of Materials Science and Engineering, University of Shanghai for Science and Technology, Shanghai 200093, China. E-mail: cxpeng@usst.edu.cn

^cShanghai Innovation Institute for Materials, Shanghai 200444, China

^dState Key Laboratory of Advanced Chemical Power Sources, Guizhou Meiling Power Sources Co. Ltd., Zunyi, Guizhou 563003, China

† Electronic supplementary information (ESI) available. See DOI: 10.1039/c8ta10554e

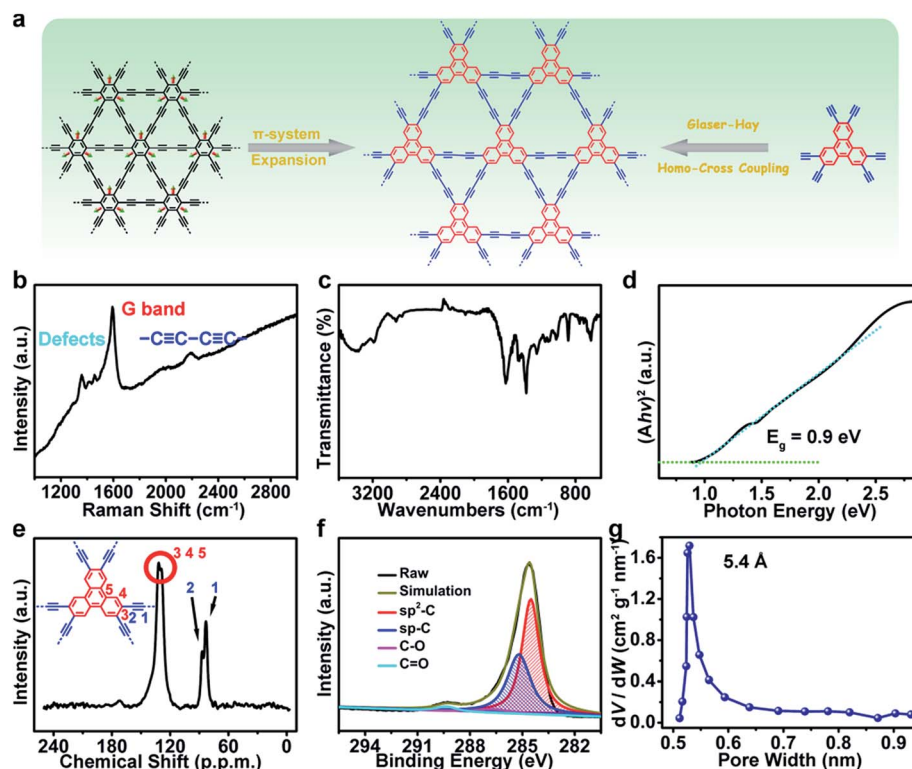


Fig. 1 The typical motif design (a) and characterization of bulk TP-COP (b–g). (b) Raman spectrum, (c) FT-IR, (d) energy band gap, (e) solid-state NMR spectrum, (f) C 1s XPS spectrum, and (g) pore distribution of bulk TP-COP.

continuous TP-COP films, which can be considered quasi-monolayer and multilayer films. The homogenous solution synthetic protocol of TP-COP allows easy wrapping onto carbon nanotubes (CNT) *in situ*, forming TP-COP/CNT composites. Due to the expanded sp^2 moieties and enlarged uniform pores, TP-COP/CNT as the anode material of lithium-ion batteries manifests remarkable reversible capacity up to 1624 mA h g^{-1} , high rate capability (590 mA h g^{-1} at 8.0 A g^{-1}) and good recyclability.

Results and discussion

TP-COP was synthesized through the alkyne–alkyne Glaser–Hay cross-coupling of the monomer HETP. Fig. 1a shows the synthesis procedure, and detailed HETP characterizations are shown in the ESI (Fig. S1–S6[†]). Under argon atmosphere, acetone solution of HETP (0.4 mg mL^{-1} , 50 mL) was slowly added to 50 mL acetone solution of $\text{Cu}(\text{OAc})_2$ -pyridine complex (2 mmol L^{-1}) in the dark using a syringe pump. Then, the homogenous mixture was stirred at $60 \text{ }^\circ\text{C}$ for 24 hours. Upon completion of polymerization, bulk TP-COP was formed as a black solid after washing thoroughly (please see ESI[†] for details).

Bulk TP-COP is insoluble in common organic solvents, indicating that it is the polymerized product. The TP-COP powder was expected to comprise a 2D graphene-like framework with TP cores, which were linked by butadiynes, as illustrated in Fig. 1a. The polymerization of HETP monomers by Glaser–Hay cross-coupling resulted in the formation of

butadiyne units in TP-COP (Fig. 1a). The Raman spectrum of TP-COP in Fig. 1b clearly shows the characteristic peak (2185 cm^{-1}) of conjugated butadiyne linkages. In addition, Raman peaks at 1358 cm^{-1} and 1593 cm^{-1} were ascribed to the D and G bands, respectively, which are typical spectral features of conjugated carbon frameworks.^{19,29} The loss of $\equiv\text{C-H}$ vibration peak at 3288 cm^{-1} in the Fourier transform infrared (FT-IR) spectrum of TP-COP also confirmed the coupling between $\equiv\text{C-H}$ groups (Fig. 1c and S7[†]). Due to the formation of the conjugated framework in TP-COP, the ultraviolet-visible (UV-Vis) absorption spectrum of TP-COP red-shifted by 152 nm compared with that of the monomer (Fig. S8[†]). The optical band gap of TP-COP was estimated to be 0.9 eV (Fig. 1d) by the following relation: $\alpha \propto (\hbar\nu - E_g)^{1/2}/\hbar\nu$.³⁰ This band gap was slightly smaller than that of GDY.³¹

More detailed characterization of TP-COP was obtained by solid-state NMR spectroscopy. As shown in Fig. 1a, the structure of TP-COP contains five kinds of carbon species. Two carbon species (1# and 2#) are butadiyne linkers and the other three (3#–5#) are aromatic TP cores (inset of Fig. 1e). Clearly, two peaks at 84.9 and 88.1 ppm are found in NMR spectra (Fig. 1e) and their chemical shifts proved them as the carbon species of butadiyne linker (1# and 2#). In the aromatic range, there were only two peaks, corresponding to three aromatic carbon species of TP core (carbon species of 3#–5#), which could be attributed to the signal overlap due to the similar chemical environments of the aromatic carbons and the relatively low resolution of solid-state NMR. Notably, these peaks in the aromatic range of

TP-COP shifted downfield compared to those of the HETP monomer (Fig. S9†), suggesting the formation of an expanded π -conjugated framework.³² The assignable NMR signals validated the well-defined chemical structure of TP-COP at least in the local range, as displayed in Fig. 1a.

The chemical environments of these carbon species were also checked by XPS, as shown in Fig. 1f. The C 1s envelope of TP-COP can be deconvoluted into two major subpeaks of 284.7 eV and 285.4 eV, which are assigned to the sp^2 - and sp -hybridized carbons in the framework of TP-COP, respectively.³³ The peak area ratio of sp^2 - and sp -hybridized carbons is close to 3 : 2, which indicates that TP units link with others by butadiyne as the expected structure (Fig. 1a). The tail in C 1s, attributed to C–O at 287.5 eV and C=O at 288.4 eV, is due to slight oxidation of C \equiv C bond, which has also been observed in other alkyne-rich COPs.^{22,34}

The structure of TP-COP implied the construction of uniform pores by butadiyne linkers and TP nodes (Fig. 1a). Argon adsorption–desorption experiments of TP-COP were carried out. It can be seen from Fig. S10† that the adsorption quantity of Ar sharply increases at very low P/P_0 due to mass of adsorption of Ar in the micropores of TP-COP. The continued adsorption of Ar and H3-type hysteresis loop at relatively higher pressures indicate multilayer adsorption, and this can be ascribed to the existence of mesopores and macropores, which are also observed in the TEM image of TP-COP (Fig. S13d and e†). The argon adsorption–desorption isotherm of bulk TP-COP (Fig. S10a†) exhibits BET surface area of 241.2 m² g⁻¹. A sharp distribution of pore size at 5.4 Å was observed for bulk TP-COP (Fig. 1g and S10b†), indicating a highly ordered porous structure, which can be ascribed to the well-defined local structure of TP-COP. The measured pore size is smaller than the pore size of monolayer TP-COP, which could result from the staggered packing of TP units in multi-layered TP-COP (Fig. S11†). Meanwhile, the staggered packing also blocked the small pores in the structure.

The 2D layered COP tended to stack into a multilayer laminar structure due to strong interlayer π – π interactions.³⁵ As expected, the layered structure existed in solid state TP-COP. X-ray diffraction (XRD) revealed a broad peak at 23.4° for bulk TP-COP (Fig. S12†), corresponding to interspacing of 3.8 Å. This result is consistent with the high resolution transmission electron microscopy (HRTEM) images (Fig. 2a and S13c†). Both XRD and HRTEM results suggested poor crystallinity of bulk TP-COP, which resulted from the irreversibility of the C–C coupling reaction.^{27,36} Other 2D COPs linked by C–C coupling also presented such kind of partial or poor crystallinity.^{20,33,37}

The scanning electron microscopy (SEM) and TEM images of bulk TP-COP also showed layered stacking morphology (Fig. 2a, b and S13†), which suggests the exfoliation of bulk TP-COP into few-layer sheets. After ultrasonication in dimethyl formamide (DMF) for 10 min (please see ESI† for details), a colloidal dispersion of the exfoliated TP-COP (E-TP-COP) in DMF was formed, exhibiting a clear Tyndall effect. This suspension was stable for at least a month without any precipitate formation (inset of Fig. 2f). Unlike the results for bulk TP-COP (Fig. 2b and S13a†), the SEM image of E-TP-COP presented flat morphology

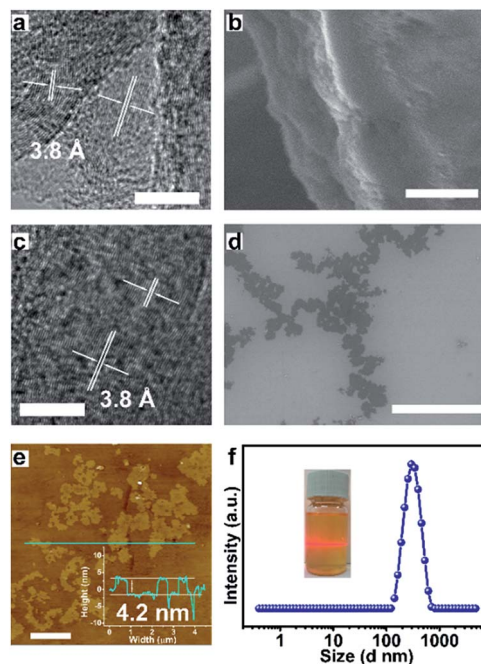


Fig. 2 (a) HRTEM and (b) SEM images of bulk TP-COP. (c) HRTEM and (d) SEM images of E-TP-COP nanosheets. (e) AFM image of E-TP-COP nanosheets. Inset: height profile along the line. (f) DLS analysis of E-TP-COP nanosheets. Inset: optical image of E-TP-COP nanosheets in DMF solution, indicating a strong Tyndall effect. The scale bars in (a)–(e) indicate distances of 10 nm, 5 μ m, 10 nm, 500 nm and 1 μ m, respectively.

with small thickness (Fig. 2d), highlighting the 2D features. The HRTEM image (Fig. 2c) confirmed the ultrathin graphene-like morphology of E-TP-COP as compared to that of the bulk powder. The crystal lattices can still be identified in the HRTEM images (Fig. 2c), indicating that E-TP-COP comprised few-layer nanosheets.

The atomic force microscopy (AFM) image of E-TP-COP nanosheets (Fig. 2e) also revealed flat graphene-like morphology on the silicon wafer. The thickness of the nanosheets was measured to be 4.2 nm with slight variations, which corresponded to the few-layered structure of TP-COP. Notably, the lateral size of the nanosheets ranges from 150 to 700 nm, leading to a high aspect ratio, thereby confirming their 2D layered features. The dynamic light scattering (DLS) measurements indicated an average size of about 0.4 μ m in DMF solution (Fig. 2f), which was in agreement with the SEM, HRTEM, and AFM results (Fig. 2c–e).

Although few-layered TP-COP can be prepared by mechanical exfoliation of the bulk powder, the size of E-TP-COP nanosheets was in nano-scale without thickness control. Interfacial polymerization at the liquid/liquid interface has been proven as an effective strategy for fabricating 2D-COP with enlarged size and controllable thickness.³⁸ Very recently, Hiroshi Nishihara and co-workers reported the synthesis of large-area TP-GDY films with thickness of hundreds of nanometers.³³ We modified the catalysts and solvents for interfacial polymerization (ESI, Fig. S14†) and achieved quasi-monolayer and multilayer TP-

COP films. In addition, the thickness of the TP-COP films was well regulated by the concentration of HETP monomer and the catalytic complex (ESI^\dagger).

The chemical structures of the obtained films were also characterized by Raman, FT-IR, XPS, and HRTEM techniques, and the results were in good agreement with those of bulk TP-COP (Fig. S15 and S16, \dagger please see ESI for details). The optical microscopy (OM), SEM and AFM images of all the films (Fig. S17 \dagger) revealed a continuous lateral size larger than $100\ \mu\text{m}$ and a smooth surface with few contaminants. Notably, using a dilute HETP solution ($10\ \mu\text{g mL}^{-1}$) and catalytic copper acetate ($100\ \mu\text{mol L}^{-1}$), a continuous film of TP-COP ($10\text{--}100$) with thickness of $0.9\ \text{nm}$ was synthesized, which can be considered as the monolayer of TP-COP (Fig. 3). The observation of a few wrinkles even in the monolayer TP-COP film suggests its good mechanical strength.

The porous and 2D π -conjugated structure of TP-COP suggests its application as a lithium storage material for lithium batteries. However, bulk TP-COP shows low electronic conductivity, which is quite common for COPs.⁷ Therefore, we performed the hybridization of TP-COP and carbon nanotubes (CNT, ESI^\dagger). The TP-COP and CNT composite (TP-COP/CNT) can be formed *in situ* by suspending CNT in a polymerization solution, where TP-COP grows on CNT owing to π - π interactions between TP units and CNT (Fig. 4a). By filtration, free-standing TP-COP/CNT films can be obtained.

Next, the electrochemical properties of the free-standing TP-COP/CNT film were evaluated (please see details in ESI^\dagger). Fig. 4b and c show the typical gravimetric charge–discharge profiles and the corresponding dQ/dV curves of the TP-COP/CNT film in the voltage range of $0.005\text{--}3.0\ \text{V}$, respectively. Three reduction peaks at ~ 1.5 , ~ 0.7 , and $\sim 0.2\ \text{V}$ and three oxidation peaks at ~ 0.5 , ~ 1.1 , and $\sim 2.0\ \text{V}$ are observed, which are ascribed to the lithiation/delithiation of Li within extended π -conjugated TP-COP. As proposed in the literature,³⁶ lithium atoms can bind to the peripheral H atoms of TP units at about $0.7\text{--}1.5\ \text{V}$; they are adsorbed above the center of the 6-C hexagon and located near butadiyne in the hexagonal pores at about $0.2\ \text{V}$. In this study, a pair of strong redox peaks is observed at a voltage near $0.2\ \text{V}/0.5\ \text{V}$, indicating considerable Li insertion above the benzene ring and the butadiyne moiety in TP-COP. In addition, no clear changes were observed in the sequence of the dQ/dV curves during the initial cycles, revealing highly reversible redox reactions and stable cycling performance of the TP-COP/CNT film (Fig. 4c).

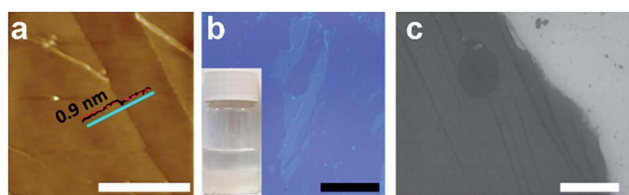


Fig. 3 AFM image (a), OM image (b), and SEM image (c) of quasi-single layer TP-COP film. Inset in (b) shows the optical photograph of interfacial polymerization. The scale bars in (a)–(c) indicate distances of 5, 25, and $10\ \mu\text{m}$, respectively.

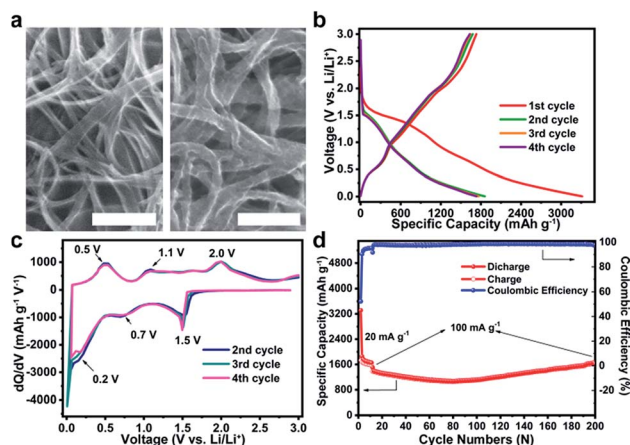


Fig. 4 TP-COP/CNT composite as the anode material of a lithium battery. (a) SEM images of CNT (left) and TP-COP/CNT (right). (b) Gravimetric charge–discharge profiles at a current of $20\ \text{mA g}^{-1}$. (c) The corresponding dQ/dV curves. (d) Cycling performance at a current density of $100\ \text{mA g}^{-1}$. The scale bars in (a) indicate distance of $250\ \text{nm}$.

The cycling performance of TP-COP-based electrode was investigated and is shown in Fig. 4d. The TP-COP/CNT film delivers an initial discharge capacity of $\sim 3313\ \text{mA h g}^{-1}$ under a current of $20\ \text{mA g}^{-1}$ and a capacity of $\sim 1732\ \text{mA h g}^{-1}$ in the reverse process, giving low initial coulombic efficiency of 52%. The high irreversible capacity loss can be ascribed to the consumptive formation of solid electrolyte interphase (SEI) layers on the high surface area of TP-COP/CNT film. After initial stabilization at a low current ($20\ \text{mA g}^{-1}$), the TP-COP/CNT film battery exhibits a high reversible capacity of $1395\ \text{mA h g}^{-1}$ at a current of $100\ \text{mA g}^{-1}$ (the specific capacity contribution of TP-COP in the TP-COP/CNT film is estimated to be $1844\ ((1395 - 522 \times 0.34)/0.66)\ \text{mA h g}^{-1}$ based on the electrochemical evaluation of the CNT substrate from S17 to S21 \dagger). Interestingly, reversible capacity shows an upward trend with cycles. After 200 cycles, the delivery capacity rises gradually to $\sim 1624\ \text{mA h g}^{-1}$. The increase in delivery capacity is due to more absorption of lithium ions into the expanded interlamellar space of the layered COP, which occurs with cycling.³⁵ In addition, high coulombic efficiency of around 98% for the TP-COP/CNT film with cycling demonstrates strong coupling interaction between TP-COP and CNT, which firmly stabilizes the electrode and effectively facilitates electron transport *via* conductive CNT. The outstanding battery performance of the TP-COP/CNT film is much greater than the theoretical capacities of $372\ \text{mA h g}^{-1}$ for graphite and $\sim 500\ \text{mA h g}^{-1}$ for CNT, suggesting that the TP-COP/CNT film can serve as a promising anode material for high-capacity lithium-ion batteries.

In addition, the TP-COP/CNT film-based electrode exhibits excellent rate capability. As shown in Fig. 5, it presents high reversible capacities of *ca.* 1395, 1213, 1103, 985, 876 and $718\ \text{mA h g}^{-1}$ at rates of 0.1, 0.2, 0.5, 1.0, 2.0 and $5.0\ \text{A g}^{-1}$, respectively. Even as the current density approaches $8.0\ \text{A g}^{-1}$, which is 80 times larger than initial $0.1\ \text{A g}^{-1}$, a capacity of $590\ \text{mA h g}^{-1}$ is obtained. This capacity is larger than that of

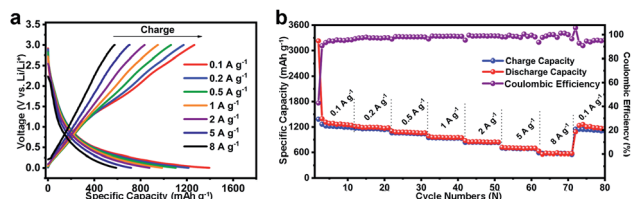


Fig. 5 The rate performance of the TP-COP/CNT film for a lithium battery. (a) Gravimetric charge–discharge profiles at different current loadings. (b) The rate capability at currents of 0.1, 0.2, 0.5, 1, 2, 5, and 8 A g⁻¹.

conventional graphite anode materials. Moreover, when the rate returns to the initial current, the composite electrode still exhibits high capacity retention of 88.5% after 70 cycles, suggesting good rate capability.

The superior electrochemical performance of the TP-COP/CNT film is attributed to its unique features: (i) the extended π -conjugated system within TP-COP and coupling with conductive CNT enhance the electric conductivity and facilitate electron transport; (ii) the hierarchical abundant pores of the TP-COP/CNT film endow the electrode with a high specific surface area, giving rise to large reversible capacity and high energy density. Furthermore, the ordered vertically aligned pores shorten the diffusion pathway and effectively accelerate Li⁺ transport, which result in high rate performance and power density.

Conclusions

Using hexaethynyltriphenylene as the building unit, we synthesized 2D TP-COP by Glaser–Hay cross-coupling in a homogenous solution or at the interface of liquids. The structure of TP-COP was well characterized. Few-layered TP-COP can be obtained by mechanical exfoliation or interface polymerization. As the anode material of a lithium battery, TP-COP shows reversible capacity up to 1624 mA h g⁻¹, good rate performance (590 mA h g⁻¹ at 8.0 A g⁻¹) and good recycling ability, which can be ascribed to the porous and 2D π -conjugated structure of TP-COP. The easy and tunable synthesis of TP-COP and its good electronic activity promise its further applications in energy storage and conversion.

Conflicts of interest

There are no conflicts to declare.

Acknowledgements

The authors thank the financial support from the National Natural Science Foundation of China (21771155, 21721001, 21875141), the Ministry of Science and Technology of China (2017YFA0204902), Shanghai Pujiang Program (18PJ1409000), Opening Project of State Key Laboratory of Advanced Chemical Power Sources (SKL-ACPS-C-23), and the Fundamental Research Funds for the Central Universities (20720180035).

Notes and references

- 1 K. S. Novoselov, A. K. Geim, S. V. Morozov, D. Jiang, Y. Zhang, S. V. Dubonos, I. V. Grigorieva and A. A. Firsov, *Science*, 2004, **306**, 666–669.
- 2 A. K. Geim and K. S. Novoselov, *Nat. Mater.*, 2007, **6**, 183–191.
- 3 A. Gupta, T. Sakhivel and S. Seal, *Prog. Mater. Sci.*, 2015, **73**, 44–126.
- 4 X. Cai, Y. Luo, B. Liu and H.-M. Cheng, *Chem. Soc. Rev.*, 2018, **47**, 6224–6266.
- 5 C. Tan, X. Cao, X.-J. Wu, Q. He, J. Yang, X. Zhang, J. Chen, W. Zhao, S. Han, G.-H. Nam, M. Sindoro and H. Zhang, *Chem. Rev.*, 2017, **117**, 6225–6331.
- 6 Z. Xiang, Q. Dai, J.-F. Chen and L. Dai, *Adv. Mater.*, 2016, **28**, 6253–6261.
- 7 Z. Xiang, D. Cao and L. Dai, *Polym. Chem.*, 2015, **6**, 1896–1911.
- 8 J. W. Colson and W. R. Dichtel, *Nat. Chem.*, 2013, **5**, 453–465.
- 9 J. Sakamoto, J. van Heijst, O. Lukin and A. D. Schlüter, *Angew. Chem., Int. Ed.*, 2009, **48**, 1030–1069.
- 10 P. Peng, Z. Zhou, J. Guo and Z. Xiang, *ACS Energy Lett.*, 2017, **2**, 1308–1314.
- 11 Z. Xiang, Y. Xue, D. Cao, L. Huang, J.-F. Chen and L. Dai, *Angew. Chem., Int. Ed.*, 2014, **53**, 2433–2437.
- 12 Z. Xiang and D. Cao, *J. Mater. Chem. A*, 2013, **1**, 2691–2718.
- 13 Q. Fan, J. M. Gottfried and J. Zhu, *Acc. Chem. Res.*, 2015, **48**, 2484–2494.
- 14 X. H. Liu, C. Z. Guan, D. Wang and L. J. Wan, *Adv. Mater.*, 2014, **26**, 6912–6920.
- 15 Y.-Q. Zhang, N. Kepčija, M. Kleinschrodt, K. Diller, S. Fischer, A. C. Papageorgiou, F. Allegretti, J. Björk, S. Klyatskaya, F. Klappenberger, M. Ruben and J. V. Barth, *Nat. Commun.*, 2012, **3**, 1286.
- 16 H.-Y. Gao, H. Wagner, D. Zhong, J.-H. Franke, A. Studer and H. Fuchs, *Angew. Chem., Int. Ed.*, 2013, **52**, 4024–4028.
- 17 Q. Sun, L. Cai, H. Ma, C. Yuan and W. Xu, *ACS Nano*, 2016, **10**, 7023–7030.
- 18 H.-Y. Gao, D. Zhong, H. Mönig, H. Wagner, P.-A. Held, A. Timmer, A. Studer and H. Fuchs, *J. Phys. Chem. C*, 2014, **118**, 6272–6277.
- 19 W. Liu, X. Luo, Y. Bao, Y. P. Liu, G.-H. Ning, I. Abdelwahab, L. Li, C. T. Nai, Z. G. Hu, D. Zhao, B. Liu, S. Y. Quek and K. P. Loh, *Nat. Chem.*, 2017, **9**, 563–570.
- 20 Z. Xiang, D. Cao, L. Huang, J. Shui, M. Wang and L. Dai, *Adv. Mater.*, 2014, **26**, 3315–3320.
- 21 N. Huang, P. Wang and D. Jiang, *Nat. Rev. Mater.*, 2016, **1**, 16068.
- 22 G. Li, Y. Li, H. Liu, Y. Guo, Y. Li and D. Zhu, *Chem. Commun.*, 2010, **46**, 3256–3258.
- 23 C. Huang, Y. Li, N. Wang, Y. Xue, Z. Zuo, H. Liu and Y. Li, *Chem. Rev.*, 2018, **118**, 7744–7803.
- 24 C. Kuang, G. Tang, T. Jiu, H. Yang, H. Liu, B. Li, W. Luo, X. Li, W. Zhang, F. Lu, J. Fang and Y. Li, *Nano Lett.*, 2015, **15**, 2756–2762.
- 25 R. Liu, H. Liu, Y. Li, Y. Yi, X. Shang, S. Zhang, X. Yu, S. Zhang, H. Cao and G. Zhang, *Nanoscale*, 2014, **6**, 11336–11343.

- 26 Y. Zhao, J. Wan, H. Yao, L. Zhang, K. Lin, L. Wang, N. Yang, D. Liu, L. Song, J. Zhu, L. Gu, L. Liu, H. Zhao, Y. Li and D. Wang, *Nat. Chem.*, 2018, **10**, 924–931.
- 27 J. He, N. Wang, Z. Yang, X. Shen, K. Wang, C. Huang, Y. Yi, Z. Tu and Y. Li, *Energy Environ. Sci.*, 2018, **11**, 2893–2903.
- 28 S. Zhang, H. Liu, C. Huang, G. Cui and Y. Li, *Chem. Commun.*, 2015, **51**, 1834–1837.
- 29 J. Dong, X. Li, K. Zhang, Y. Di Yuan, Y. Wang, L. Zhai, G. Liu, D. Yuan, J. Jiang and D. Zhao, *J. Am. Chem. Soc.*, 2018, **140**, 4035–4046.
- 30 T. Yu, B. Lim and Y. Xia, *Angew. Chem., Int. Ed.*, 2010, **49**, 4484–4487.
- 31 N. Ketabi, T. M. Tolhurst, B. Leedahl, H. Liu, Y. Li and A. Moewes, *Carbon*, 2017, **123**, 1–6.
- 32 W. B. Wan, S. C. Brand, J. J. Pak and M. M. Haley, *Chem.–Eur. J.*, 2000, **6**, 2044–2052.
- 33 R. Matsuoka, R. Toyoda, R. Shiotsuki, N. Fukui, K. Wada, H. Maeda, R. Sakamoto, S. Sasaki, H. Masunaga, K. Nagashio and H. Nishihara, *ACS Appl. Mater. Interfaces*, 2018, DOI: 10.1021/acsami.1028b00743.
- 34 J. Zhou, X. Gao, R. Liu, Z. Xie, J. Yang, S. Zhang, G. Zhang, H. Liu, Y. Li, J. Zhang and Z. Liu, *J. Am. Chem. Soc.*, 2015, **137**, 7596–7599.
- 35 Z. Lei, Q. Yang, Y. Xu, S. Guo, W. Sun, H. Liu, L.-P. Lv, Y. Zhang and Y. Wang, *Nat. Commun.*, 2018, **9**, 576.
- 36 J. He, N. Wang, Z. Cui, H. Du, L. Fu, C. Huang, Z. Yang, X. Shen, Y. Yi, Z. Tu and Y. Li, *Nat. Commun.*, 2017, **8**, 1172.
- 37 H. Yang, S. Zhang, L. Han, Z. Zhang, Z. Xue, J. Gao, Y. Li, C. Huang, Y. Yi, H. Liu and Y. Li, *ACS Appl. Mater. Interfaces*, 2016, **8**, 5366–5375.
- 38 R. Dong, T. Zhang and X. Feng, *Chem. Rev.*, 2018, **118**, 6189–6235.